IEEE Access
Multidisciplinary | Rapid Review | Open Access Journal

Received February 14, 2019, accepted February 27, 2019, date of publication March 11, 2019, date of current version March 29, 2019.

Digital Object Identifier 10.1109/ACCESS.2019.2904097

Infrared LEDs-Based Pose Estimation With Underground Camera Model for Boom-Type Roadheader in Coal Mining

WENJUAN YANG[1,2], XUHUI ZHANG[1,2], (Member, IEEE), HONGWEI MA[1,2], AND GUANG-MING ZHANG[3]

[1]School of Mechanical Engineering, Xi'an University of Science and Technology, Xi'an 710054, China
[2]Shaanxi Key Laboratory of Mine Electromechanical Equipment Intelligent Monitoring in Shaanxi, Xi'an 710054, China
[3]Faculty of Engineering and Technology, General Engineering Research Institute, Liverpool John Moores University, Liverpool L3 3AF, U.K.

Corresponding author: Wenjuan Yang (1805909145@qq.com)

This work was supported in part by the National Green Manufacturing System Integration Project under Grant 2017-327, in part by the Shaanxi Innovative Talent Plan Project under Grant 2018TD-032, and in part by the Key R&D Project in Shaanxi under Grant 2018ZDCXL-GY-06-04.

ABSTRACT Accurate and reliable pose estimation of a boom-type roadheader is of great importance in order to maintain the efficiency of automatic coal mining. The stability and accuracy of conventional measurement methods are difficult to be guaranteed on account of vibration noise, magnetic disturbance, electrostatic interference, and other factors in an underground environment. In this paper, a vision-based non-contact measurement method for cutting-head pose estimation is presented, which deploy a 16-point infrared LED target on the boom-type roadheader to tackle the low-illumination, high-dust, and complicated background. By establishing a monocular vision measurement system, the cutting-head pose is estimated through processing the LED target images obtained from an explosion-proof industrial camera mounted on the roadheader. After analyzing the measurement mechanism, an underground camera model based on the equivalent focal length is built to eliminate refraction errors caused by the two-layer glasses for explosion-proof and dust removal. Then, the pose estimation processes, including infrared LEDs feature point extraction, spot center location, and an improved P4P method based on dual quaternions, are carried out. The influence factors of cutting-head pose estimation accuracy are further studied by modeling, and the error distribution of the main parameters is investigated and evaluated. The numerical simulation and experimental evaluation are designed to verify the performance of the proposed method. The results show that the pose estimation error is in line with the numerical prediction, achieving the requirements of cutting-head pose estimation in underground roadway construction in the coal mine.

INDEX TERMS Vision measurement, infrared LEDs, pose estimation, underground camera model, total accuracy error, boom-type roadheader.

I. INTRODUCTION

Intelligent drivage is the only way to realize automatic operation in comprehensive tunnel working face, and an accurate self-localization of cutting path is of key importance to tunneling automation and control technology. However, the long-distance acquisition of cutting-head pose estimation is still an unresolved problem in coal mining.

At present, a variety of pose detection methods for coal mining equipment have been studied, such as inclinometer, gyroscope, GPS, INS, UWB, laser guide, etc. Due to strong vibration, high dust, noise and other factors in underground working environment, these measurement methods have some deficiencies. The angular sensor based methods [1]–[3] are installed at the rotating joint or lifting joint of the cutting arm, and vibration condition accelerates the sensors damage. The measurement accuracy and reliability degrades very quickly after a short period of using in the working condition. Three-axis acceleration sensors will engender fairly great error due to mechanical vibration noise as well. The magnetostrictive displacement sensor is subject to electromagnetic interference, resulting in

The associate editor coordinating the review of this manuscript and approving it for publication was Shih-Wei Lin.

low accuracy. Moreover, an infrastructure dependent sensor is necessary for machine fuselage self-localization. Tunneling roadway is a narrow and long-distance space, which located at 300 $\sim$ 800 meters underground, hence, there exist no GPS signals in coal mine. The positioning accuracy of UWB-based method would degrade when the distance between the UWB base stations and the roadheader expands during construction of roadway tunneling [4], [5], and the antenna sensitivity is the main requirement of its application in tunneling roadway. Inertial navigation are infrastructure independent, which can offer high-accuracy pose estimation but are sensitive to accumulated drift due to double integration [6]–[8]. Laser based methods [9]–[11] have high-accuracy localization, however, it have a very high requirement for the quality of 3D laser scanners. In recent years, vision measurement technology has become a hot research topic in pose estimation for its advantages of non-contact measurement, high precision and good stability.

The vision measurement technology has been applied in a certain range in coal mines. Vision-based method is based on the spatial relationship between the 2D image and the 2D or 3D feature points in the scene [12]. For extremely low illuminance and dense-dust in tunnel working face, non-marker based vision methods are prone to failure due to blurred images captured, which lead to the difficulty in tracking of scene features and obtaining accurate pose estimation. Marker based pose estimation [12], [13] is an effective and accurate approach to obtain six-dimensional cutting-head pose estimation, and it evolves the extraction of markers image and the pose estimation algorithm, which can be typically estimated by homography decomposition or by solving the perspective-n-point (PnP) problem. The PnP methods include iterative and non-iterative methods. LHM [14], DLT [15] and HOMO [16] are the classical non-iterative methods, but are sensitive to noise. Lepetit *et al.* [17] proposed a non-iterative algorithm known as EPnP, which is efficient but inaccurate when the number of points is equal to 4 or 5. RPnP [18] works well when the number of points is less than 6 but does not work well when the depth is big.

This paper proposes a novel infrared LEDs-based pose estimation system that significantly improves cutting-head position accuracy and reliability in tunneling face. The main contribution of this paper are as follows: 1)Taking the angular mounting offset into the consideration, an underground camera model based on the equivalent focal length was built to eliminate refraction errors, which was triggered by the two layer glasses for explosion-proof and dust removal. 2) Multiple infrared LEDs were adopted to tackle the coal mine environment. Considering the feature points might be occluded by water mists and dense-dust, the 3D coordinates of the target are calculated based on the least square fitting with the detected infrared LEDs on the same line, and dual quaternion is introduced to obtain optimal solution. 3) By modeling and simulation, the pose estimation accuracy and the cutting-head position error distribution under the influence of the main parameters are investigated. 4) The simulation evaluation and the experimental evaluation are designed to verify the performance of the proposed method and the established system.

The remainder of this work is organized as follows: Section II describes the vision-based cutting-head pose estimation system design and the camera marker network. Section III puts forward the underground camera model. Section IV introduces the cutting-head pose estimation algorithm. Section V builds the cutting-head pose estimation error model. Section VI carries out numerical analysis and the experimental evaluation of the proposed method. Section VII presents the experimental results of the established vision-based cutting-head pose estimation system. Finally, the full text is summarized and discussed in Section VIII.

II. INFRARED LEDs-BASED VISION MENSEARMENT SYSTEM FOR BOOM-TYPE ROADHEADER

The tunneling machine carries out tunneling work according to requirements, the fuselage coordinates is acquired by the fusion of multiple sensors. As shown in Fig. 1, the cutting head move along scheduled trajectory (the red route on the coal wall), and the pose estimation of the cutting-head is realized by a vision-based method. The camera mounted on the machine body collects the infrared target image. Besides, the infrared LEDs-based target is mounted on the cutting-arm in case of the potential collision during excavation processing.

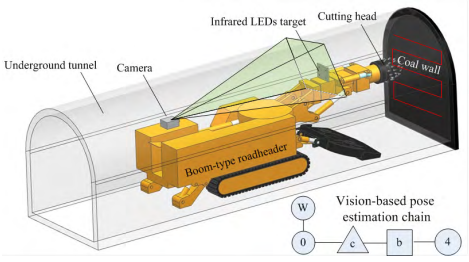

FIGURE 1. Schematic of Boom-type roadheader pose estimation.

As shown in Fig. 2a, the vision-based pose measurement system involves seven coordinate frames, the camera coordinate frame $O_cX_cY_cZ_c$, the machine body coordinate frame $O_0X_0Y_0Z_0$, the rotary joints coordinate frame of cutting part $O_1X_1Y_1Z_1$, the lift joints coordinate frame of cutting part $O_2X_2Y_2Z_2$, the expansion joints coordinate frame of cutting part $O_3X_3Y_3Z_3$, the cutting-head coordinate frame $O_4X_4Y_4Z_4$, the target coordinate frame $O_bX_bY_bZ_b$. The movements of the rotary joints and the lift joints are shown in Fig. 2b and 2c.

A camera-marker graph can be used to abstract the cutting-head pose estimation system. The camera-marker network is shown in Fig. 3. It involves object coordinates frame and the relative relationship between two object coordinates frames, which are illustrated with nodes and edges, respectively. The graph provides a theoretical frame for the cutting-head pose estimation, which is estimated through the camera observation, kinematics, and calibration here.

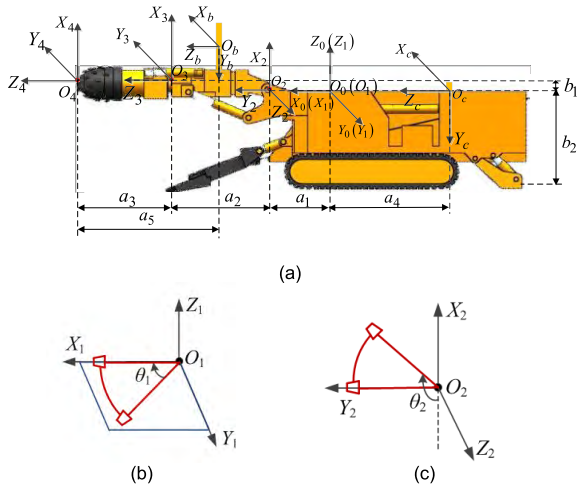

FIGURE 2. Coordinate systems of Boom-type roadheader. (a) The coordinate systems. (b) The rotate angle. (c) The pitch angle.

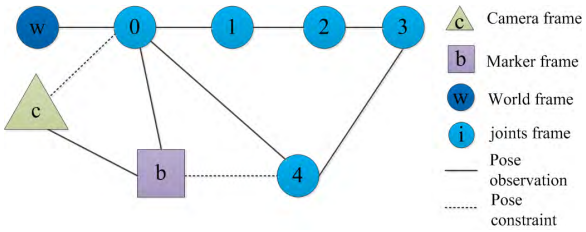

FIGURE 3. Camera-marker graph for Boom-type roadheader.

There are three chains exist in this graph to obtain the coordinate parameters of the cutting head on Boom-type roadheader.

A. CHAIN-1: VISION-BASED POSE ESTIMATION CHAIN O_0-O_c-O_b-O_4

The vision-based pose estimation chain involves four coordinate frames as shown in Fig. 3. The transformation matrix $\mathbf{M}_c^b$ is acquired based on the infrared LEDs-based pose estimation algorithm, which is described in section IV. The rigid transformation relationship between the camera and machine body $\mathbf{M}_0^c$, and the transformation relationship between the target and cutting-head $\mathbf{M}_b^4$, are pre-calibrated in accordance with the chain-3. Hence, vision-based cutting-head pose can be estimated based on the following equation:

$$\mathbf{M}_0^4 = \mathbf{M}_0^c \mathbf{M}_c^b \mathbf{M}_b^4 \tag{1}$$

where $\mathbf{M}_0^c$ represent the transformation relation between the machine body and camera frames; $\mathbf{M}_b^4$ represent the transformation relation between the target and cutting-head coordinate frames; $\mathbf{M}_c^b$ represent the transformation relation between the camera and target coordinate frames; $\mathbf{M}_0^4$ represent the transformation relation between the machine body and the cutting-head coordinate frames.

B. CHAIN-2: KINEMATIC CHAIN O_0-O_1-O_2-O_3-O_4

As shown in Fig. 3, kinematic positive solution can be used to present the cutting-head coordinates in the machine body coordinate frame:

$$\mathbf{M}_0^4 = \mathbf{M}_0^1 \mathbf{M}_1^2 \mathbf{M}_2^3 \mathbf{M}_3^4 \tag{2}$$

where, $\mathbf{M}_0^1$ represent the transformation relation between the machine body and the rotary joints coordinate frames; $\mathbf{M}_1^2$ represent the transformation relation between the rotary joints and the lift joints coordinate frames; $\mathbf{M}_2^3$ represent the transformation relation between the lift joints and expansion joints coordinate frames; $\mathbf{M}_3^4$ represent the transformation relation between the expansion joints and cutting-head coordinate frames.

C. CHAIN-3: CALIBRATION CHAIN O_0-O_b-O_4

The transformation relation $\mathbf{M}_0^b$ between the machine body and target coordinate frames can be calibrated by a total station or a visual tracking system. Then combined with the kinematic chain, the rigid transformation matrix of $\mathbf{M}_b^4$ can be calculated using the following equation

$$\mathbf{M}_b^4 = \left(\mathbf{M}_0^b\right)^{-1} \cdot \mathbf{M}_0^4 \tag{3}$$

Hence, the rigid transformation matrix of $\mathbf{M}_0^c$ can be obtained based on the following equation

$$\mathbf{M}_0^c = \mathbf{M}_0^4 \cdot \left(\mathbf{M}_b^4\right)^{-1} \cdot \left(\mathbf{M}_c^b\right)^{-1} \tag{4}$$

III. UNDERGROUND CAMERA MODEL

Considering the requirements of explosion-proof and dust removal in the coal mining, the camera is fixed in a specially designed apparatus as shown in Fig. 4. The dust removal is used to clean dust and mists from the outer glass, which is driven by the DC motor with reduction gear. The camera is mounted in the cylinder-shaped explosion-proof apparatus.

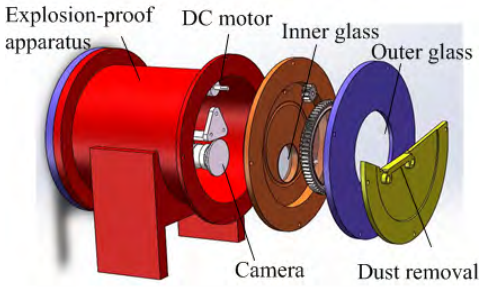

FIGURE 4. Explosion-proof apparatus with dust remover.

Vision-based measurement is in accordance with collinearity, however, which is hard to satisfy in underground camera imaging system because the lights must pass through two explosion-proof glasses. Hence, the underground camera model based on equivalent focal length [19], [20] is proposed, which take the apparatus interface as the virtual image plane and the origin at distance F-ΔF as the virtual perspective center. As shown in Fig. 5.

The underground camera model is illustrated by the following parameters: α, the refraction angle; β, the incidence angle; η, the incidence angle; and τ, the refraction angle; f, the

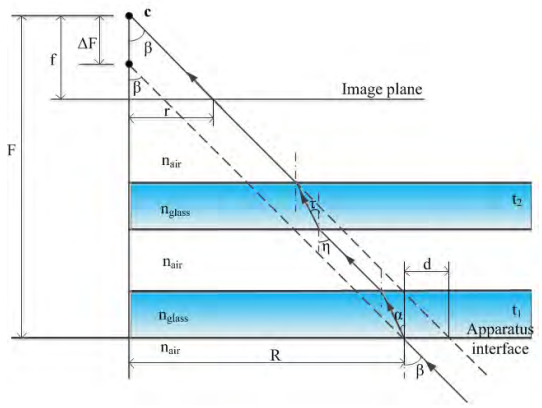

FIGURE 5. Mine camera ray diagram when the optical axis is orthogonal to the two layer of glasses. The incoming ray first refracted at the outer glass interface, then refracted at the inner glass interface, and reach the focal plane.

actual focal length; r, the radial distance; d, the incoming ray offset on the inner glass interface and outer glass interface; F, the distance between the apparatus interface and the actual perspective center; R, the distance between the incident point and the camera's optical axis; ΔF, the offset of virtual perspective center.

A. ORTHOGONALITY

Assuming that the optical axis is orthogonal to the double layers of glass, the relative refractive index of the air and glass is n, the offset of incoming ray on the double layers of glass interface can be expressed as

$$d = t_1 (\tan\beta - \tan\alpha) + t_2 (\tan\eta - \tan\tau) \tag{5}$$

With the relation

$$R = \frac{rF}{f} - d \tag{6}$$

ΔF can be expressed as From Eq. (7) and (8),

$$\Delta F = F - \frac{R}{\tan\beta} = (t_1 + t_2)\left(1 - \frac{f}{\sqrt{(n^2-1)r^2 + n^2 f^2}}\right) \tag{7}$$

or

$$\Delta F(\beta) = (t_1 + t_2)\left(1 - \frac{\cos\beta}{\sqrt{n^2 - 1 + \cos^2\beta}}\right) \tag{8}$$

The image coordinates in the virtual imaging system are:

$$x' = f' \frac{\langle \mathbf{r_1}, \mathbf{p}\rangle - \langle \mathbf{r_1}, \mathbf{c}+\Delta\mathbf{c}\rangle}{\langle \mathbf{r_3}, \mathbf{p}\rangle - \langle \mathbf{r_3}, \mathbf{c}+\Delta\mathbf{c}\rangle}, \quad y' = f' \frac{\langle \mathbf{r_2}, \mathbf{p}\rangle - \langle \mathbf{r_2}, \mathbf{c}+\Delta\mathbf{c}\rangle}{\langle \mathbf{r_3}, \mathbf{p}\rangle - \langle \mathbf{r_3}, \mathbf{c}+\Delta\mathbf{c}\rangle} \tag{9}$$

where $\mathbf{c}$ is the camera coordinates, $\mathbf{p}$ is the object coordinates, $\Delta\mathbf{c}$ is $\mathbf{r_3}\Delta$F, the $\mathbf{r}_i$ (i = 1, 2, 3) are the row vectors of the rotation matrix between the object and camera frames, with the following relation

$$[x', y', f']^T = \left[\frac{F-\Delta F}{f}x, \frac{F-\Delta F}{f}y, F-\Delta F\right]^T \tag{10}$$

Eq. (9) can be expressed as

$$x = f\frac{\langle \mathbf{r_1}, \mathbf{p}\rangle - \langle \mathbf{r_1}, \mathbf{c}\rangle}{\langle \mathbf{r_3}, \mathbf{p}\rangle - \langle \mathbf{r_3}, \mathbf{c}\rangle - \Delta F}, \quad y = f\frac{\langle \mathbf{r_2}, \mathbf{p}\rangle - \langle \mathbf{r_2}, \mathbf{c}\rangle}{\langle \mathbf{r_3}, \mathbf{p}\rangle - \langle \mathbf{r_3}, \mathbf{c}\rangle - \Delta F} \tag{11}$$

The modified collinearity equation introduce the additional parameters t_1, t_2 and n in the mine camera imaging system.

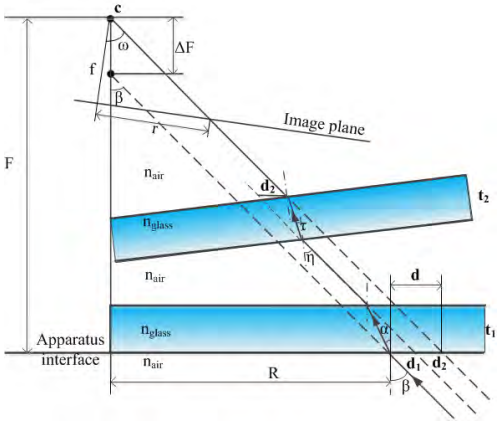

FIGURE 6. Mine camera ray diagram for a more general situation when the optical axis is not orthogonal to the double layer of glasses.

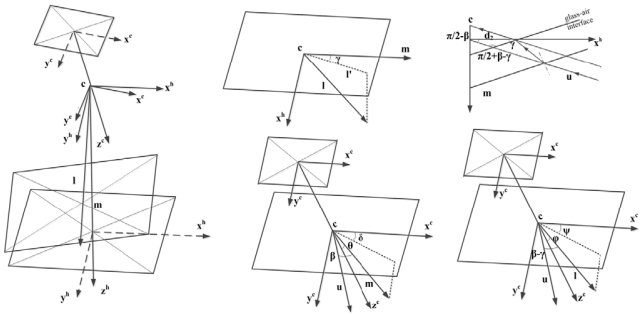

FIGURE 7. A diagram of the underground camera imaging system when the optical axis is not orthogonal to the double layer of glasses.

B. NON-ORTHOGONALITY

Considering angular mounting offset, the simplified model for a more general situation is established as shown in Fig. 6 and Fig. 7. The angular offset between the camera's optical axis and the outer layer glass interface is described by: the angle between the camera's optical axis and the outer layer glass interface normal, θ, and its projection direction on the image plane with respect to the camera's x-axis, δ. In the same way, the angular offset between the camera's optical axis and the inner layer glass interface normal is described by the angle between the camera's optical axis and the interface normal, φ, and its projection direction on the image plane with respect to the camera's x-axis, ψ.

The mounting offset can be expressed by the transformation matrix $\mathbf{M}_c^h$ from the camera to the outer layer glass frames and the transformation matrix $\mathbf{M}_c^l$ from the camera to the inner glass frames.

$$\mathbf{x}^h = \mathbf{M}_c^h \mathbf{x}^c, \quad \mathbf{M}_c^h = \mathbf{R}_y(\theta)\,\mathbf{R}_z(\delta) \tag{12}$$

$$\mathbf{x}^l = \mathbf{M}_c^l \mathbf{x}^c, \quad \mathbf{M}_c^l = \mathbf{R}_y(\varphi)\,\mathbf{R}_z(\psi) \tag{13}$$

where $\mathbf{x}^c$ is the vector in the camera frame, $\mathbf{x}^h$ is the same vector in the outer layer glass frame, and $\mathbf{x}^l$ is the same vector in the inner layer glass frame.

As $\mathbf{m}$, the third row of $\mathbf{M}_c^h$, is the vector of virtual optical axis in mine camera imaging system, $\mathbf{u}$ is the vector from the actual perspective center to the actual image point, and $\mathbf{l}$, the third row of $\mathbf{M}_c^l$, is the normal vector of inner layer glass interface, so

$$\cos\beta = \frac{(\mathbf{m})^{\mathrm{T}}\mathbf{u}}{\|\mathbf{u}\|}, \quad \cos\eta = \frac{(\mathbf{l})^{\mathrm{T}}\mathbf{u}}{\|\mathbf{u}\|} \tag{14}$$

the incoming ray offset d_1 on the x_h-axis of virtual imaging system is

$$d_1 = t_1(\tan\beta - \tan\alpha) \tag{15}$$

assuming κ is the angle between the incoming ray offset vector on the inner glass interface and the projection of the inner glass interface on the plane formed by $\mathbf{m}$ and $\mathbf{u}$ (the incoming ray offset along the plane normal is assumed to be negligible here), with the geometric relations illustrated in Fig. 7, the incoming ray offset d_2 on the x_h-axis of virtual imaging system can be obtained using the following equation.

$$\frac{t_2 \cdot (\tan\eta - \tan\tau)\cdot\cos\kappa}{\sin(\pi/2 - \beta)} = \frac{d_2}{\sin(\pi/2 + \beta - \gamma)} \tag{16}$$

ΔF can be expressed as

$$\Delta F(\beta) = d/\tan\beta, \quad d = d_1 + d_2 \tag{17}$$

with $\mathbf{z}$, the third row of $(\mathbf{M}_c^h)^{-1}\mathbf{m}^{\mathbf{T}}\Delta$F is the vector in the z-axis of camera frame, and $\mathbf{x}$, the first row of $(\mathbf{M}_c^h)^{-1}\mathbf{m}^{\mathbf{T}}\Delta$F is the vector in the x-axis of camera frame

$$x = f\frac{\tan\omega}{\tan\beta}\cdot\frac{\langle\mathbf{r_1},\mathbf{p}\rangle - \langle\mathbf{r_1},\mathbf{c}\rangle - \mathbf{x}}{\langle\mathbf{r_3},\mathbf{p}\rangle - \langle\mathbf{r_3},\mathbf{c}\rangle - \mathbf{z}},$$
$$y = f\frac{\tan\omega}{\tan\beta}\cdot\frac{\langle\mathbf{r_2},\mathbf{p}\rangle - \langle\mathbf{r_2},\mathbf{c}\rangle - \mathbf{x}}{\langle\mathbf{r_3},\mathbf{p}\rangle - \langle\mathbf{r_3},\mathbf{c}\rangle - \mathbf{z}} \tag{18}$$

Hence, when ΔF is substituted into Eq. (18), a more general modified collinearity equation for underground camera imaging system is obtained.

IV. POSE ESTIMATION

In accordance with the vision-based pose estimation chain, this section gives the cutting-head pose estimation method including the center positioning of feature points and improved pose estimation algorithm based on dual quaternion.

A. CENTER POSITIONING OF FEATURE POINTS

Coal mine tunneling working face is of low illumination. Moreover, pose estimation will failure in the case of partial occlusion of measured infrared LEDs. Therefore, the system adopts multiple infrared LEDs as the feature points. As shown in Fig. 8, a 16-point infrared LEDs target is designed to prevent feature points from being occluded by water mists, dense-dust and other mine equipment. In addition, a narrow-band filter is installed in front of the camera lens, it is beneficial and high-efficiency for extracting and positioning of feature points in complex background.

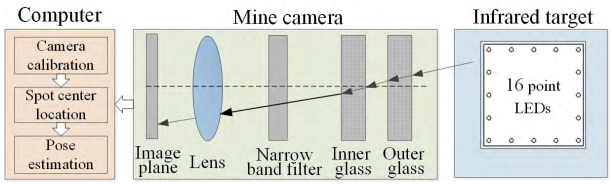

FIGURE 8. Schematic diagram of pose estimation based on 16-point infrared LEDs target.

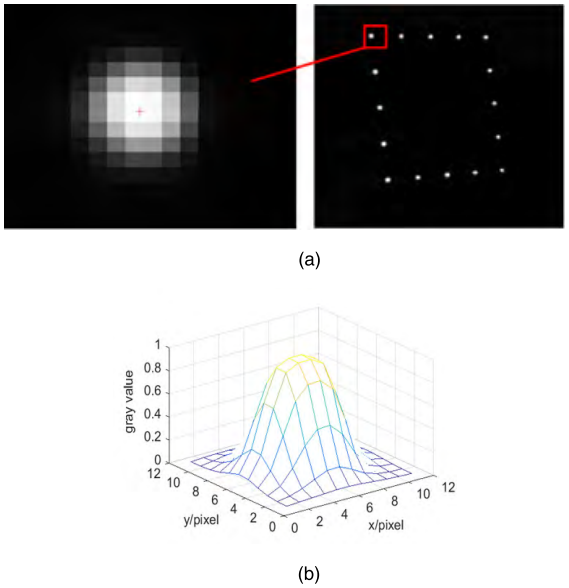

FIGURE 9. The image of infrared LEDs and its intensity distribution. (a) The collected image of infrared LEDs. (b) Intensity distribution.

By optimizing the luminous intensity of infrared LEDs, the diameter of the region of interest (ROI) is about 10 pixels. The grayscale distribution of ROI are shown in Fig. 9, the shape of the ROI is approximately circular, the gray value of ROI present a symmetric descending distribution from the center to the edge, and the gray value of pixels in the ROI is significantly higher than that of the background.

Typical target location algorithms are the weighted centroid method, least-squares template matching and curved surface fitting method [21]–[23]. The non-iterative spot center location based on Gaussian fitting algorithm [24] is used for the infrared LEDs-based target location in our system. It is superior to the standard Gaussian surface fitting method

since it is with a prominent advantage in operation efficiency and can meet the requirement for fast spot center location. The pixel grayscale distribution of the infrared LED can be expressed in the following equation.

$$f\left(x_i, y_j\right) = \frac{I_0}{2\pi\sigma_x\sigma_y} \exp\left(-\frac{(x_i - x_0)^2}{2\sigma_x^2}\right) \exp\left(-\frac{\left(y_j - y_0\right)^2}{2\sigma_y^2}\right) \tag{19}$$

where I_0 is total energy of the spot; (x_0, y_0) represents the spot center, (x_i, y_j) is pixel gray values; (σ_x, σ_y) is the standard deviation of the 2D Gaussian distribution.

The Eq. (19) can be expressed in matrix form as follows:

$$f\left(\mathbf{x}, \mathbf{x}_0\right) = \frac{I_0}{2\pi\sqrt{\det \mathbf{R}}} \exp\left[-\frac{1}{2}\left(\mathbf{x} - \mathbf{x}_0\right)^{\mathrm{T}} R^{-1}\left(\mathbf{x} - \mathbf{x}_0\right)\right] \tag{20}$$

$$\mathbf{R} = \begin{bmatrix} \sigma_x^2 & \rho\sigma_x\sigma_y \\ \rho\sigma_x\sigma_y & \sigma_y^2 \end{bmatrix} \tag{21}$$

where $\mathbf{x} = [x_i, y_i]^{\mathrm{T}}$ is pixel coordinate; $\mathbf{x}_0 = [x_0, y_0]^{\mathrm{T}}$ is the spot center location; ρ is the correlation between the x-axis and y-axis direction

Let

$$\mathbf{D} = \begin{bmatrix} d_{11} & d_{12} \\ d_{21} & d_{22} \end{bmatrix}, \quad \mathbf{D} = \mathbf{R}^{-1} \tag{22}$$

For $\mathbf{D}$ is real symmetric matrix, $d_{12} = d_{21} = d_1$, $\mathbf{x}_0^{\mathrm{T}}\mathbf{D}$ is defined as $[a_1, a_2]$, with

$$a_0 = -\ln\frac{I_0}{2\pi\sqrt{\det \mathbf{R}}} + \frac{1}{2}\mathbf{x}_0^{\mathrm{T}}\mathbf{D}\mathbf{x}_0 \tag{23}$$

The Eq. (20) can be expressed in matrix form as follows:

$$\begin{bmatrix} -\ln f_1 \\ -\ln f_2 \\ \vdots \\ -\ln f_n \end{bmatrix} = \begin{bmatrix} 1 & -x & -y_1 & \frac{1}{2}x_1^2 & x_1y_1 & \frac{1}{2}y_1^2 \\ 1 & -x_2 & -y_2 & \frac{1}{2}x_2^2 & x_2y_2 & \frac{1}{2}y_2^2 \\ \vdots & \vdots & \vdots & \vdots & \vdots & \vdots \\ 1 & -x_n & -y_n & \frac{1}{2}x_n^2 & x_ny_n & \frac{1}{2}y_n^2 \end{bmatrix} \begin{bmatrix} a_0 \\ a_1 \\ a_2 \\ d_{11} \\ d_1 \\ d_{22} \end{bmatrix} \tag{24}$$

$$\mathbf{F} = \mathbf{A}\mathbf{Z} \tag{25}$$

where $\mathbf{F}$ is the logarithm matrix of pixel gray values; $\mathbf{A}$ is the sensitivity matrix; n is the number of the pixel points; $\mathbf{Z} = [a_0, a_1, a_2, d_{11}, d_1, d_{22}]^{\mathrm{T}}$

Hence, $\mathbf{Z}$ can be obtained using the least squares estimation algorithm, and the spot center location can be realized by using the following equation

$$\mathbf{x}_0 = \left(\begin{bmatrix} a_1 & a_2 \end{bmatrix}\mathbf{D}^{-1}\right)^{\mathrm{T}} \tag{26}$$

B. IMPROVED POSE ESTIMATION ALGORITHM BASED ON DUAL QUATERNION

Our improved pose estimation method is heavily affected by M A Abidi.'s P4P method [25], which is an efficient pose estimation method based on the volume measurement of tetrahedral. According to the results of above spot center location of infrared target, an improved P4P method is proposed for our roadheader pose estimation system. Assume that the distance equation from the spot center to the fitting straight line is:

$$\left|ax_i + by_i + c\right| / \sqrt{a^2 + b^2} = \left|d_i\right| \tag{27}$$

The linear equation of each side of the target can be fitted by the least square fitting with constraints.

$$L\left(a, b, c, \lambda\right) = \frac{1}{n}\left\|a\mathbf{X} + b\mathbf{Y} + c - \mathbf{D}\right\|^2 + \lambda\left(a^2 + b^2 - 1\right), a^2 + b^2 = 1 \tag{28}$$

The line fitting error can be expressed as:

$$\min_{a,b,c} e\left(a, b, c\right) = \min_{a,b,c}\frac{1}{n}\left\|\left(\mathbf{X}, \mathbf{Y}\right)\left(a, b\right)^{\mathrm{T}} + c - \mathbf{D}\right\|^2 \tag{29}$$

The maximum allowable error $e_{\max}$ is introduced to judge whether the result of line fitting is acceptable or not. On this basis, the pixel coordinates of the four vertices of the target are calculated through the intersection of two adjacent lines. Then, P4P algorithm [25] is used to calculate spatial three-dimensional coordinate of four vertex coordinates for the target in the camera coordinate system, and the dual quaternion is introduced to establish the error objective function to obtain optimal solution, which transfer the P4P problem into an optimization problem.

Suppose the three-dimensional coordinate of feature points in the target coordinate system are $\mathbf{P}_{bi}(x_{bi}, y_{bi}, z_{bi})$, and the three-dimensional coordinate of feature points in the camera coordinate system are $\mathbf{P}_{ci}(x_{ci}, y_{ci}, z_{ci})$. The transform relation between the target coordinate system and the camera coordinate system can be expressed as

$$\mathbf{P}_{ci} = \mathbf{R}_b^c\mathbf{P}_{bi} + \mathbf{T}_b^c, \quad (i = 1, 2, 3, 4) \tag{30}$$

The rotation matrix $\mathbf{R}_b^c$ and translation matrix $\mathbf{T}_b^c$ can be respectively expressed by Eq. (31) and (32) using dual quaternion, and $\mathbf{Q}(\mathbf{r})$ and $\mathbf{W}(\mathbf{r})$ are defined in [26]:

$$\begin{bmatrix} 1 & 0 \\ 0 & \mathbf{R}_b^c \end{bmatrix} = \mathbf{Q}^{\mathrm{T}}\left(\mathbf{r}\right)\mathbf{W}\left(\mathbf{r}\right) \tag{31}$$

$$\begin{bmatrix} 0 \\ \mathbf{T}_b^c \end{bmatrix} = 2\mathbf{Q}^{\mathrm{T}}\left(\mathbf{r}\right)\mathbf{s} \tag{32}$$

Suppose actual measured value of target vertexes in the camera coordinate system are $\tilde{\mathbf{P}}_{ci}$ $(i = 1, 2, 3, 4)$. As there exist errors between the actual measured value and the theoretical value, the optimal solution of the rotation matrix $\mathbf{R}_b^c$ and

translation matrix $\mathbf{T}_b^c$ can be obtained by the error objective function as follows:

$$F\left(\mathbf{R}_b^c, \mathbf{T}_b^c\right) = \min \frac{1}{N} \sum_{i=1}^{N} \left\| \mathbf{P}_{ci} - \tilde{\mathbf{P}}_{ci} \right\|^2 \tag{33}$$

The error objective function using dual quaternion [27], [28] can be expressed as

$$F\left(\mathbf{r}, \mathbf{s}\right) = \min \frac{1}{N} \left(\mathbf{r}^{\mathrm{T}} \mathbf{G}_1 \mathbf{r} + \mathbf{s}^{\mathrm{T}} \mathbf{G}_2 \mathbf{r} + 4N \mathbf{s}^{\mathrm{T}} \mathbf{s} + \mathbf{G}_3 \right) \tag{34}$$

where

$$\mathbf{G}_1 = -\sum_{i=1}^{N} \left(\mathbf{Q}^{\mathrm{T}}\left(\mathbf{P}_{bi}\right) \mathbf{W}\left(\tilde{\mathbf{P}}_{ci}\right) + \mathbf{W}^{T}\left(\tilde{\mathbf{P}}_{ci}\right) \mathbf{Q}\left(\mathbf{P}_{bi}\right) \right)$$

$$\mathbf{G}_2 = 4 \sum_{i=1}^{N} \left(\mathbf{Q}\left(\mathbf{P}_{bi}\right) - \mathbf{W}^{T}\left(\tilde{\mathbf{P}}_{ci}\right) \right)$$

$$\mathbf{G}_3 = \sum_{i=1}^{N} \left(\mathbf{P}_{bi}^{T} \mathbf{P}_{bi} + \tilde{\mathbf{P}}_{ci}^{T} \tilde{\mathbf{P}}_{ci} \right)$$

V. CUTTING-HEAD POSE ESTIMATION ERROR MODEL

The main influence factors of the proposed pose estimation method include the image coordinates error of spot center location, the external parameters calibration error and the non-coplanar errors of infrared LEDs. This section derives the pose estimation error model of above three parameters.

A. IMAGE COORDINATES ERROR OF SPOT CENTER LOCATION

In order to study the influence of image coordinates error of the spot center location on the cutting-head pose estimation, the error transform function is deduced. Take a derivative with respect to image coordinates, carry out the Taylor series expansion, neglect the higher order term of the expansion, and reserve the first degree as the measurement error of feature points' 3D coordinates in the camera coordinate system.

$$\begin{aligned} \delta X_{ci} &= \frac{\partial X_{ci}}{\partial u} \delta u_i + \frac{\partial X_{ci}}{\partial v} \delta v_i, \\ \delta Y_{ci} &= \frac{\partial Y_{ci}}{\partial u} \delta u_i + \frac{\partial Y_{ci}}{\partial v} \delta v_i \end{aligned} \tag{35}$$

where δu_i, δv_i are the spot center location errors, $i = 1,2,3,4$.

The error transfer function between the spot center location error $\delta\mathbf{P}$ and the 3D coordinate error $\delta\mathbf{W}$ can be defined as

$$\delta \mathbf{W} = \mathbf{E}_{wp} \delta \mathbf{P} \tag{36}$$

where

$$\mathbf{E}_{wp} = \begin{bmatrix} \frac{\partial X_{c1}}{\partial u_1} & \frac{\partial X_{c1}}{\partial v_1} & \cdots & \frac{\partial X_{c1}}{\partial u_4} & \frac{\partial X_{c1}}{\partial v_4} \\ \vdots & \vdots & \vdots & \vdots & \vdots \\ \frac{\partial Y_{c4}}{\partial u_1} & \frac{\partial Y_{c4}}{\partial v_1} & \cdots & \frac{\partial Y_{c4}}{\partial u_4} & \frac{\partial Y_{c4}}{\partial v_4} \end{bmatrix}$$

$$\delta \mathbf{P} = \left(\delta u_1, \delta v_1, \delta u_2, \delta v_2, \delta u_3, \delta v_3, \delta u_4, \delta v_4\right)^{\mathrm{T}}$$

$$\delta \mathbf{W} = \left(\delta X_{c1}, \delta Y_{c1}, \delta X_{c2}, \delta Y_{c2}, \delta X_{c3}, \delta Y_{c3}, \delta X_{c4}, \delta Y_{c4}\right)^{\mathrm{T}}$$

The relationship between the pitch and rotate angle of the cutting-head and the 3D coordinate of feature points can be defined as

$$\begin{aligned} f\left(pitch, rotate, X_{c1}, Y_{c1}, Z_{c1}, X_{c2}, Y_{c2}, Z_{c2}, X_{c3}, Y_{c3}, Z_{c3},\right. \\ \left. X_{c4}, Y_{c4}, Z_{c4}\right)^{\mathrm{T}} = 0 \end{aligned} \tag{37}$$

So the Jacobian matrix of Eq. (37) can be expressed as

$$\mathbf{J}_{f1} = \begin{bmatrix} \frac{\partial (pitch)}{\partial X_{c1}} & \frac{\partial (pitch)}{\partial Y_{c1}} & \frac{\partial (pitch)}{\partial Z_{c1}} & \cdots & \frac{\partial (pitch)}{\partial Y_{c4}} & \frac{\partial (pitch)}{\partial Z_{c4}} \\ \frac{\partial (rotate)}{\partial X_{c1}} & \frac{\partial (rotate)}{\partial Y_{c1}} & \frac{\partial (rotate)}{\partial Z_{c1}} & \cdots & \frac{\partial (rotate)}{\partial Y_{c4}} & \frac{\partial (rotate)}{\partial Z_{c4}} \end{bmatrix} \tag{38}$$

Set $\mathbf{E}_{p1} = \left(\mathbf{J}_{f1}^{\mathrm{T}} \mathbf{J}_{f1}\right)^{-1} \mathbf{J}_{f1}^{\mathrm{T}}$

The error transfer function between the pitch and rotate angle errors and the 3D coordinate errors of feature points can be defined as

$$\delta \mathbf{A} = \mathbf{E}_{p1} \delta \mathbf{W} \tag{39}$$

where

$$\delta \mathbf{A} = \left(\delta\left(pitch\right), \delta\left(rotate\right)\right)$$

The relationship between the pitch and rotate angle and the cutting-head position

$$f\left(pitch, rotate, X, Y, Z\right) = 0 \tag{40}$$

The Jacobian matrix of (40)

$$\mathbf{J}_f = \begin{bmatrix} \frac{\partial X}{\partial\left(pitch\right)} & \frac{\partial X}{\partial\left(rotate\right)} \\ \frac{\partial Y}{\partial\left(pitch\right)} & \frac{\partial Y}{\partial\left(rotate\right)} \\ \frac{\partial Z}{\partial\left(pitch\right)} & \frac{\partial Z}{\partial\left(rotate\right)} \end{bmatrix} \tag{41}$$

Set $\mathbf{E}_p = \left(\mathbf{J}_f^{\mathrm{T}} \mathbf{J}_f\right)^{-1} \mathbf{J}_f^{\mathrm{T}}$

The error transfer function between the position error and the pitch and rotate angle error can be expressed as

$$\delta \mathbf{T} = \mathbf{E}_p \delta \mathbf{A} \tag{42}$$

where $\delta\mathbf{T} = \left(\delta X, \delta Y, \delta Z\right)$

B. EXTERNAL PARAMETERS CALIBRATION ERROR

For the external parameters calibration error, we mainly consider the rotation error of $\mathbf{R}_b^4$ between the target and cutting-head coordinate frames,

$$\mathbf{R}_b^4 = \left[\theta_x, \theta_y, \theta_z\right]$$

The error transfer function between the pitch and rotate angle of cutting-head and the rotation error of $\mathbf{R}_b^4$ can be defined as

$$\begin{aligned} \delta\left(pitch\right) &= \frac{\partial\left(pitch\right)}{\partial\theta_x} \delta\theta_x + \frac{\partial\left(pitch\right)}{\partial\theta_y} \delta\theta_y + \frac{\partial\left(pitch\right)}{\partial\theta_z} \delta\theta_z \\ \delta\left(rotate\right) &= \frac{\partial\left(rotate\right)}{\partial\theta_x} \delta\theta_x + \frac{\partial\left(rotate\right)}{\partial\theta_y} \delta\theta_y + \frac{\partial\left(rotate\right)}{\partial\theta_z} \delta\theta_z \end{aligned} \tag{43}$$

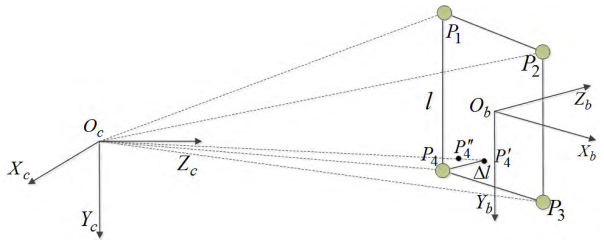

FIGURE 10. Actual imaging position of non-coplanar feature point.

where $\delta\theta_x$, $\delta\theta_y$ and $\delta\theta_z$ are the rotation error between the target and cutting-head coordinate frames.

The relationship between the pitch and rotate angle error and the rotation error of $\mathbf{R}_b^4$ can be expressed as

$$\delta\mathbf{A} = \mathbf{E}_{p2}\delta\mathbf{E} \tag{44}$$

where,

$$\delta\mathbf{E} = \left[\delta\theta_x, \delta\theta_y, \delta\theta_z\right]^{\mathrm{T}}$$
$$\mathbf{E}_{p2} = \begin{bmatrix} \frac{\partial\,(pitch)}{\partial\theta_x} & \frac{\partial\,(pitch)}{\partial\theta_y} & \frac{\partial\,(pitch)}{\partial\theta_z} \\ \frac{\partial\,(rotate)}{\partial\theta_x} & \frac{\partial\,(rotate)}{\partial\theta_y} & \frac{\partial\,(rotate)}{\partial\theta_z} \end{bmatrix}$$

Similarly, the effect of calibration error on the cutting-head position accuracy can be obtained by Eq. (40), (41) and (42).

C. NON-COPLANAR ERRORS OF INFRARED LEDs

The pose measurement results are related to the installation error of the feature points. The effect of non-coplanar error on the pose estimation is analyzed in this part. As shown in Fig. 10, P_i is defined as the ideal location. Assuming that only P_4 has an error in the perpendicular direction to the plane that consists of three other feature points, P_4' is defined as the actual location, P_4'' is defined as real imaging position on the plane, l is defined as the distance between two adjacent feature points, and Δl is defined as the distance from P_4' to P_4.

In order to ascertain the real imaging position, firstly, obtain the three-dimensional coordinates of $P_{\mathrm{b}1}$, $P_{\mathrm{b}2}$, $P_{\mathrm{b}3}$ in the target coordinate frame, and determine the spatial plane, the spatial plane equation can be expressed as $Z \equiv 0$

Suppose that O_{b} is the target origin in the target space, O_c' is the camera origin in the target space. Then, ascertain the camera origin in the target space, which can be defined as

$$O_c' = \mathbf{R}_b^c \cdot O_b + \mathbf{T}_b^c \tag{45}$$

where, $\mathbf{R}_b^c$ and $\mathbf{T}_b^c$ are respectively the rotation and translation matrix between the target and camera coordinate frame, which can be obtained according to Eq. (46), where $\mathbf{M}_0^c$, $\mathbf{M}_b^4$ and $\mathbf{M}_0^4$ can be obtained in accordance with the kinematic chain and the calibration chain that illustrated in section II

$$\mathbf{M}_b^c = \left(\left(\mathbf{M}_0^c\right)^{-1}\mathbf{M}_0^4\left(\mathbf{M}_b^4\right)^{-1}\right)^{-1},$$
$$\mathbf{M}_b^c = \begin{bmatrix} \mathbf{R}_b^c & \mathbf{T}_b^c \\ 0 & 1 \end{bmatrix} \tag{46}$$

Given that $P_4' = (-l/2, l/2, \Delta l)$, according to O_c' and P_{b4}' in the target coordinate frame, a straight line is determined, and the two-point form of straight line equation expressed as

$$\frac{X - O_c'(1)}{P_{b4}'(1) - O_c'(1)} = \frac{Y - O_c'(2)}{P_{b4}'(2) - O_c'(2)} = \frac{Z - O_c'(3)}{P_{b4}'(3) - O_c'(3)} \tag{47}$$

According to Eq. (45), (46) and (47), $P_{b4}''\left(X_{b4}'', Y_{b4}'', Z_{b4}''\right)$ in the target coordinate frame can be calculated. Given that $P_{\mathrm{b}4}$ $(X_{\mathrm{b}4}, Y_{\mathrm{b}4}, 0)$, the three-dimensional coordinates of P_1, P_2, P_3 and P_4'' in the camera space can be obtained by combining with $\mathbf{R}_b^c$ and $\mathbf{T}_b^c$, the 3D coordinates error of feature points can be expressed using the following equation

$$\delta X_{b4} = \left(\mathbf{R}_b^c \cdot X_{b4}''\right) - \left(\mathbf{R}_b^c \cdot X_{b4}\right),$$
$$\delta Y_{b4} = \left(\mathbf{R}_b^c \cdot Y_{b4}''\right) - \left(\mathbf{R}_b^c \cdot Y_{b4}\right)$$
$$\delta\mathbf{W} = (0, 0, 0, 0, 0, 0, 0, 0, 0, \delta X_{b4}, \delta Y_{b4}, 0)^{\mathrm{T}} \tag{48}$$

Similarly, the effect of non-coplanar error on the cutting-head position accuracy can be obtained by combining Eq. (39) (40), (41) and (42).

VI. EVALUATION

In experimental evaluation of the environmental adaptability and spot center location accuracy, multiple SE3470-type infrared LEDs are adopted as the feature points of the target, and the wavelength of infrared LED is 880 nm. In simulation evaluation of the underground camera model, improved pose estimation algorithm and cutting-head pose error, the value range of the joint variables of cutting-head are shown in Table 1, and the camera parameters in the simulation are shown in Table 2. The rotation and translation matrix between the machine body and camera coordinate frames are set as $\mathbf{R}_0^c = (-90°, 0°, -90°)$ and $\mathbf{T}_0^c = (-1750, 0, 0)$, respectively. The rotation and translation matrix between

TABLE 1. The value range of the joint variable of cutting-head.

a_1	a_2	a_3	a_4	a_5	b_1	θ_1	θ_2
600mm	2097mm	500mm	1750mm	2000mm	150mm	-30°~30°	-30°~30°

TABLE 2. The camera parameters in simulation.

f	u_0	v_0	d_x	d_y	C_1	C_2
5 mm	640 pixel	480 pixel	0.00375 mm	0.00375 mm	1280 pixel	960 pixel

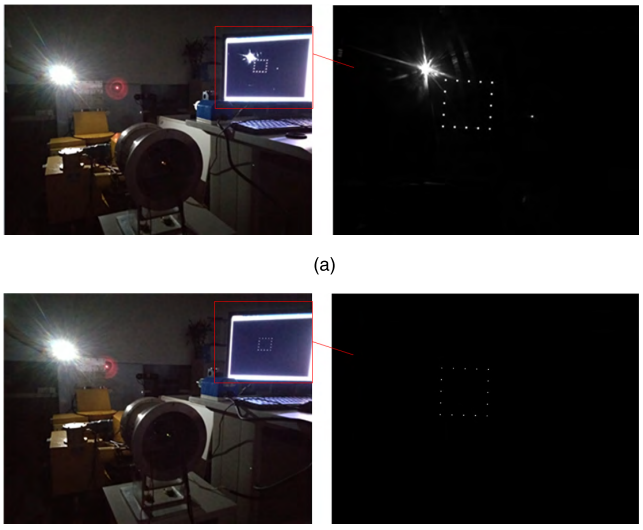

(a)

(b)

FIGURE 11. The environment adaptability experiment. (a) The image before filtering. (b) The filtered images.

TABLE 3. Intrinsic parameters of underground camera model.

underground camera parameters	value
Focal Length	800 pixel
Principal Point	[640 480]
Pixel size	3.75μm * 3.75μm
Inner glass's thickness	10 mm
Outer glass's thickness	10 mm
θ, the angle between the camera's optical axis and outer glass interface normal	10 deg
δ, the projection direction of the outer layer glass interface normal on the image plane with respect to the camera's x-axis	30 deg
φ, the angle between the camera's optical axis and inner glass interface normal	10 deg
ψ, the projection direction of the inner layer glass interface normal on the image plane with respect to the camera's x-axis	10 deg

the target and the cutting-head coordinate frames are set as $\mathbf{R}_b^4 = (0°, 0°, -90°)$ and $\mathbf{T}_b^4 = (0, 0, 2000)$, respectively. The working ranges of the pitch and rotate angle are set at $[-30°: 3°: 30°]$ and $[-30°: 3°: 30°]$, respectively. The cutting face are obtained by calculation with the kinematic chain, which is consist of 21×21 position coordinates. The 21×21 transformation matrix $\mathbf{M}_c^b$ between the camera frame and object frame are calculated by combining the kinematic chain and the vision-based pose estimation chain. The distance between the adjacent vertices of the target is set at 250 mm. The ideal image coordinates of infrared LEDs are calculated using the perspective projection model.

A. ENVIRONMENTAL ADAPTABILITY EVALUATION

Low illumination environment with mining lights, laser alignment instrument and other stray lights in driving working face were simulated in laboratory. The mine camera with a narrow-band filter placed in front of the camera lens and the

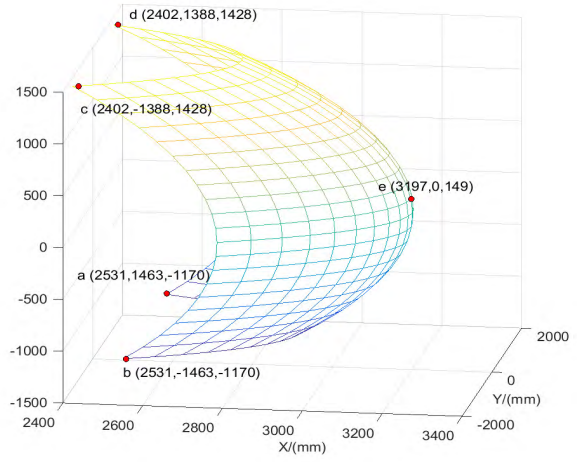

(a)

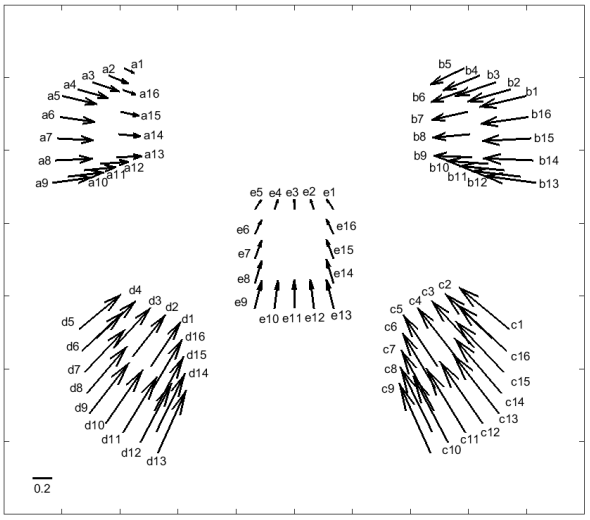

(b)

FIGURE 12. Image residuals corresponding to the five extreme positions. (a) The five extreme positions of cutting face. (b) The image residuals distribution of the 16-point Infrared LEDs target in five extreme position, the starting point of arrow represent the ideal image coordinates, the end point of arrow represent the actual image coordinate, the direction of arrow represent the actual image deviates from the ideal image coordinate, the measuring scale is 0.2 pixel.

16-point infrared LEDs-based target were specially designed. Then the mine camera was used to capture image of infrared LEDs-based target. The infrared LEDs-based target image before filtering and the filtered image are shown in Fig. 11. It can be seen from the figure that the visible light and laser alignment instrument and other stray light were eliminated through the narrow-band filter. It demonstrated that the use of mine camera and multiple infrared LEDs-based target enables the interference elimination of stray lights, simplifying the image processing process in low illumination and complex complicated background, and guaranteeing the target has the ability to be recognized and distinguished in coal mining.

TABLE 4. Image residuals of infrared LEDs.

Image residuals		a	b	c	d	e
1	Δx	0.10	-0.47	-0.52	0.30	-0.07
	Δy	-0.04	-0.08	0.34	0.36	0.09
2	Δx	0.20	-0.44	-0.47	0.33	-0.03
	Δy	-0.06	-0.10	0.36	0.34	0.09
3	Δx	0.27	-0.41	-0.43	0.36	0
	Δy	-0.07	-0.11	0.38	0.32	0.08
4	Δx	0.31	-0.38	-0.39	0.39	0.03
	Δy	-0.07	-0.12	0.40	0.30	0.08
5	Δx	0.35	-0.35	-0.34	0.42	0.07
	Δy	-0.06	-0.13	0.42	0.28	0.08
6	Δx	0.36	-0.36	-0.34	0.42	0.07
	Δy	-0.04	-0.10	0.46	0.32	0.12
7	Δx	0.37	-0.37	-0.33	0.41	0.07
	Δy	-0.01	-0.06	0.49	0.35	0.15
8	Δx	0.38	-0.38	-0.32	0.41	0.07
	Δy	0.01	-0.02	0.53	0.38	0.19
9	Δx	0.40	-0.39	-0.32	0.40	0.07
	Δy	0.04	0.01	0.56	0.41	0.23
10	Δx	0.37	-0.43	-0.36	0.38	0.03
	Δy	0.03	0.02	0.54	0.44	0.23
11	Δx	0.33	-0.46	-0.40	0.35	0
	Δy	0.02	0.03	0.52	0.46	0.23
12	Δx	0.29	-0.50	-0.43	0.32	-0.03
	Δy	0.01	0.04	0.50	0.48	0.24
13	Δx	0.26	-0.53	-0.47	0.29	-0.08
	Δy	0.01	0.05	0.48	0.51	0.24
14	Δx	0.23	-0.52	-0.48	0.29	-0.08
	Δy	-0.02	0.01	0.45	0.47	0.20
15	Δx	0.19	-0.50	-0.49	0.29	-0.08
	Δy	-0.03	-0.02	0.42	0.44	0.16
16	Δx	0.14	-0.49	-0.50	0.30	-0.08
	Δy	-0.04	-0.05	0.38	0.40	0.12

B. UNDERGROUND CAMERA MODEL EVALUATION

The effect of mine camera protecting apparatus on cutting-head pose estimation in tunneling face is evaluated based on the developed underground camera model, we make a simulation evaluation with synthetic intrinsic parameters of the underground camera as shown in Table 3. Fig. 12 illustrates image residuals of the infrared LEDs-based target at the five extreme positions of cutting surface. Table 4 shows the image residuals values of Δx in x-axis and Δy in y-axis, respectively. The results show that the angle between the camera's optical axis and the double layer glasses interface normal and the projection direction of the glass interface normal on the image plane with respect to the camera's x-axis have a great influence on the image deviation. The farther the cutting-head is from the center of the cutting surface, the greater the error. The maximum error is in the extreme position of c13, and the image residuals of infrared LED are −0.47 pixel in x-axis and 0.48 pixel in y-axis, respectively.

C. SPOT CENTER LOCATION EVALUATION

In order to evaluate the accuracy of the spot center location algorithm, the repeatability test of the location algorithm was carried out. For the same feature points in the 100 collected images, the location deviation of the spot center in the direction of X-axis and Y-axis were respectively calculated. The results of spot center location of infrared LEDs are shown in Fig. 13. The repeatability experimental results are shown in Fig. 14. It can be seen from the experimental results that the location accuracy of the feature point are within 0.03 pixel in the two directions of X-axis and Y-axis in the pixel coordinate frame.

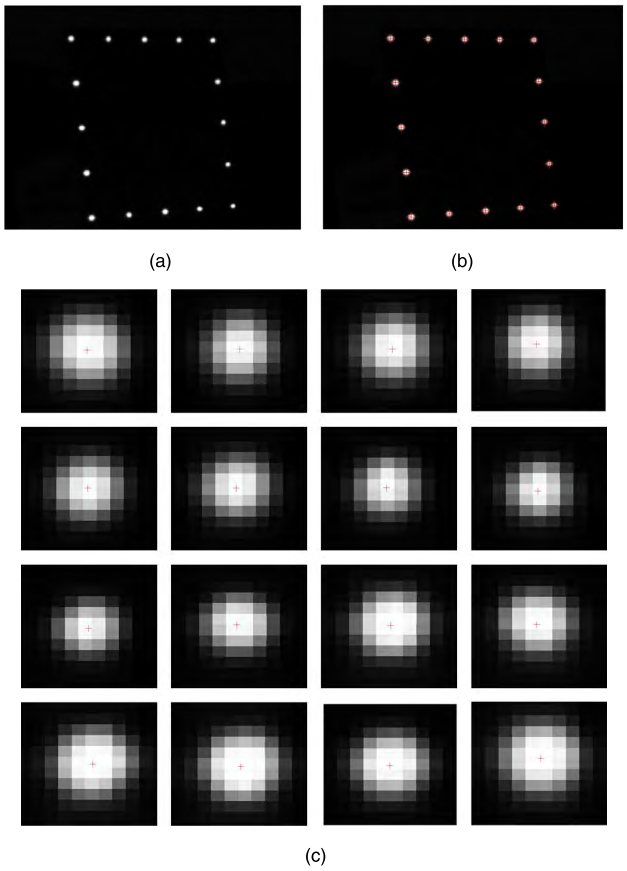

FIGURE 13. The results of spot center location. (a) The origin image. (b) The results of spot center location. (c) The results of spot center location for every ROI.

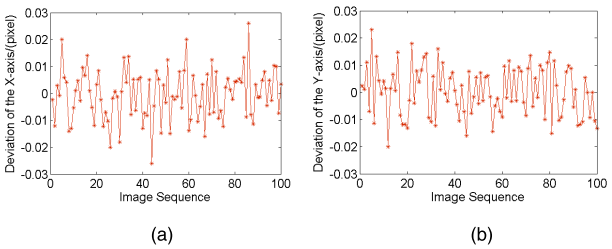

FIGURE 14. The deviation of the spot center location. (a) Deviation of the X-axis. (b) Deviation of the Y-axis.

D. IMPROVED POSE ESTIMATION EVALUATION

We give simulation evaluation on the performance of the proposed improved pose estimation algorithm with synthetic data in this section, and it was given accuracy comparison with the state-of-the-art PnP methods: HOMO, LHM, EPNP and P4P [24]. In accordance with the practical system,

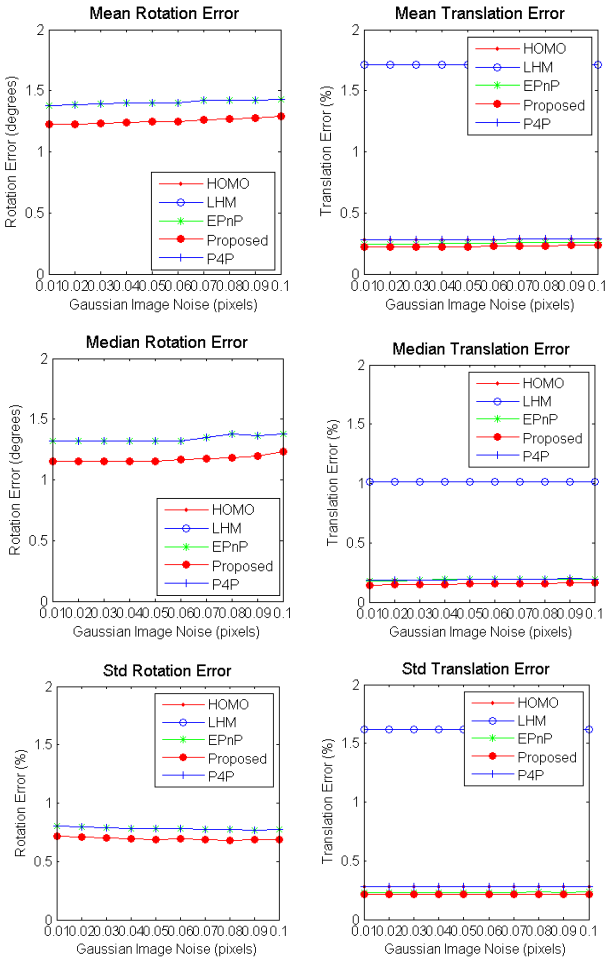

FIGURE 15. The mean, median and std rotation and translation errors.

the sixteen feature points are coplanar and distributed in the range $[-125: 62.5: 125] \times [-125: 62.5: 125] \times [0, 0]$, and they were synthesized in the target frame. For HOMO, LHM and EPNP, the four feature points were directly taken from the four vertices of the target. For our proposed improved method, the linear equations of each side of the target were firstly to be fitted by the least square fitting method and the four fitted vertices coordinates of the target were calculated through the intersection of two adjacent lines. Then, those fitted vertices and direct extracted vertices in the target frame were transformed into the camera frame using 21×21 transformation matrix $\mathbf{M}_c^b$. Finally, 2D image plane were obtained using the collinearity equations. The accuracy of above PnP methods were tested with the varying of Gaussian noise, its deviation level was varied from 0.01 to 0.1 pixels. The errors of the rotation and translation were calculated as [29]

$$e_{rot}\,(\deg rees) = \max_{k\in\{1,2,3\}} \cos^{-1}\left(r_{k,true}^{T} r_k\right) \times \frac{180}{\pi}$$
$$e_{trans}\,(\%) = \frac{\|t_{true} - t\|}{\|t\|} \times 100 \tag{49}$$

As shown in Fig. 15, the numerical simulation results demonstrated that proposed improved P4P method has better pose

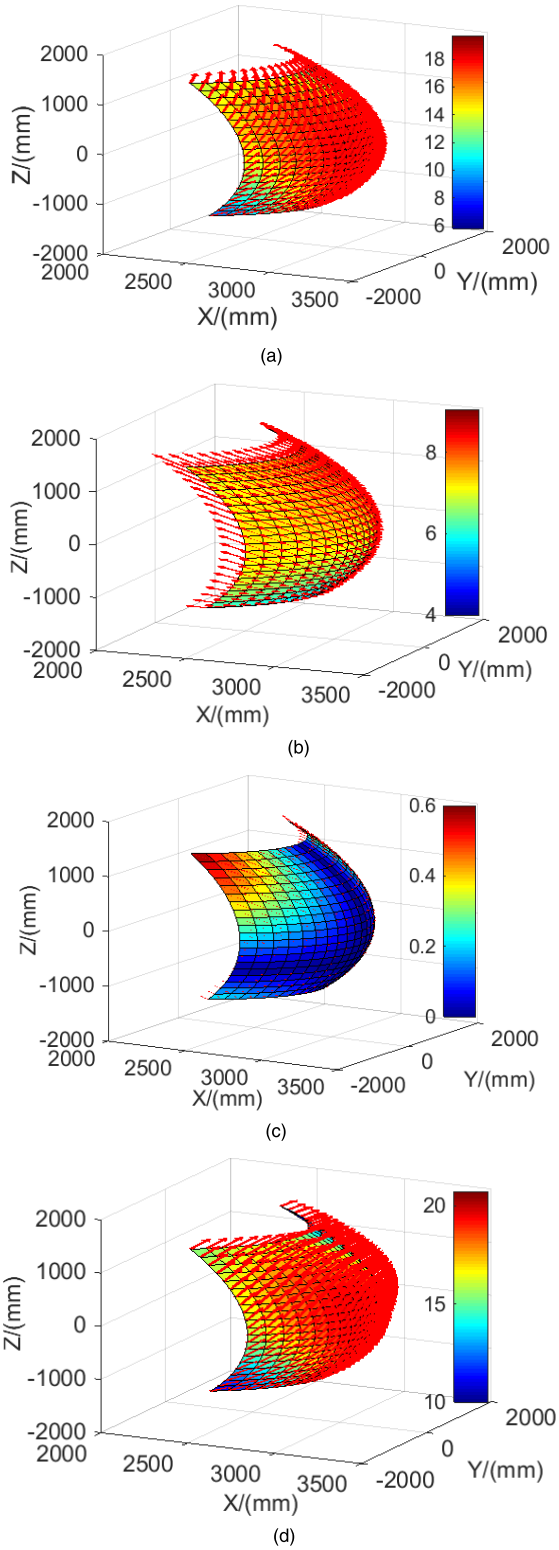

FIGURE 16. The cutting-head position error distribution under the influence of the spot center location error, the external parameter calibration error and the non-coplanar error. (a) Cutting-head position error distribution when the spot center location error is set at 0.03 pixel. (b) Cutting-head position error distribution when the external parameter calibration error is set at 0.1°. (c) Cutting-head position error distribution when the non-coplanar error is set 1 mm. (d) Cutting-head position error distribution under the influence of the above three parameters error.

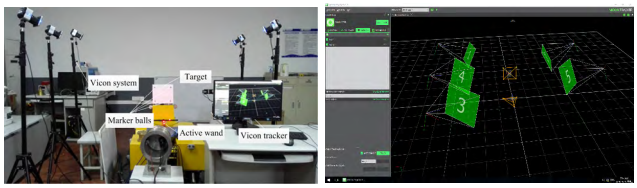

(a) (b)

FIGURE 17. The calibration system of external parameters. (a) Vicon Tracker system. (b) Software interface.

estimation accuracy in comparison with HOMO, LHM, EPNP and P4P.

E. CUTTING-HEAD POSITION ERROR EVALUATION

We conduct simulation evaluation of the cutting-head position accuracy with the established cutting-head pose estimation error model. Here the three parameters of the image coordinate errors of spot center location, the external parameters calibration error and the non-coplanar error of infrared LEDs were set at 0.03 pixel, 1 mm and 0.1°, respectively. The effect of the single parameter on the cutting-head position were analyzed when the other parameters error were set at zero.

The position error distribution were illustrated in Fig. 16. The cutting face consists of 21 × 21 data points of position coordinates. The three dimension surface represents the ideal cutting position of the roadheader. The arrow and the color bar shows error direction and error value, respectively. The maximum position error caused by the non-coplanar installation error is 0.56 mm, the maximum position error caused by the external parameter calibration error is 9.06 mm, the maximum position error caused by the spot center location error is 19.66 mm, and the maximum position error under the above three parameters is 20.72 mm.

VII. EXPERIMENTAL RESULTS

Vision-based pose estimation platform is setup as shown in Fig. 18a. The system mainly consists of Boom-type roadheader EBZ160, infrared LED SE3470, 250 mm × 250 mm rectangular target, mine explosion-proof camera MV_EM130M, PC computer and so on. Here two types of calibration are necessary for cutting-head pose estimation. The intrinsic calibration is the first thing to be done using the underground camera model in section III, in the meantime, as shown in Fig. 17, the optic motion capture system, Vicon Tracker, is adopted for the extrinsic calibration. Here, the Vicon system are consists of five cameras, an active wand, four marker balls and the Vicon tracker softerware

Adjust the cutting-head to zero-initial state when the pitch and rotate angle are zero and zero, respectively. Establish base coordinate frame by using the active wand. The measurement coordinate frame is set up using of the four marker balls which tied up on the infrared target. Here the base coordinate frame is placed in the machine body coordinate frame of $O_0X_0Y_0Z_0$ and the measurement coordinate frame is placed in target coordinate frame of $O_bX_bY_bZ_b$. It makes the acquisition of the transformation matrix of $\mathbf{M}_0^b$ simplified, which can be given directly in the Vicon motion analysis system of Vicon Tracker. Adjust the cutting-head to the other regulated states, we can obtain the accurate transformation matrix of $\mathbf{M}_0^b$ by taking the average value through multiple measurements. Then, by taking down the marker balls and collecting the infrared target images with mine explosion-proof camera, we can obtain the transformation matrix of $\mathbf{M}_b^4$ and $\mathbf{M}_0^c$ in accordance with the calibration chain, which is illustrated in section II.

On the basis of above system calibration, the correctness of the cutting-head pose estimation results were tested, and the Vicon tracker was used to measure the position of cutting-head in the machine body coordinate system. As shown in Fig. 18d, the four marker balls were tied up on the cutting-head to create the cutting-head coordinate system. As shown in Fig. 18e, the active wand was placed in the machine body coordinate system to form the base coordinate system. Therefore, the position of cutting-head in the machine body coordinate system can be given directly in the Vicon motion analysis system of Vicon Tracker, which were taken as the real value.

Control the cutting-head to move around the axis (Z_1) in rotary joints coordinate system and move around the axis (Z_2) in lift joints coordinate system, respectively. The cutting-head visual measurement system proposed in this paper and the Vicon tracker were used to measure the position of cutting-head at the same time. The measurement results are compared as shown in Fig. 19a and 19b. The trajectory measured by the proposed method is close to that measured by the Vicon tracker.

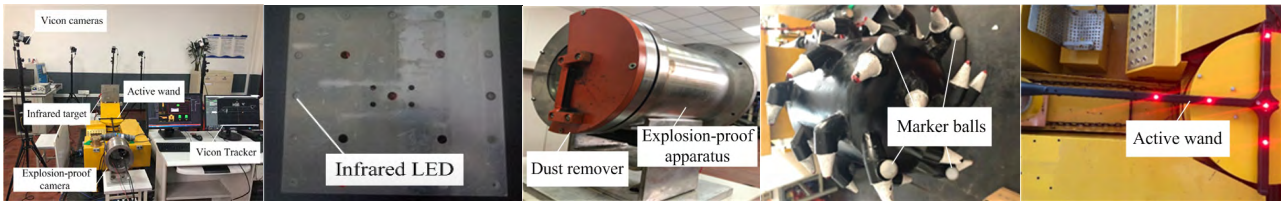

(a) (b) (c) (d) (e)

FIGURE 18. Experimental platform of visual based pose measurement system of cutting-head for Boom-type roadheader. (a) The experimental platform. (b) Infrared target. (c) Explosion-proof camera. (d) The marker balls placed on the cutting-head. (e) The active wand placed in the machine body coordinate system.

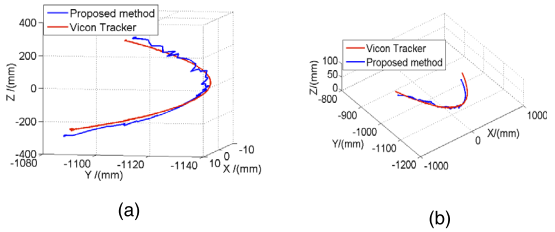

FIGURE 19. The measurement results of cutting-head position. (a) The position results when cutting-head move around the axis (Z_2) in lift joints coordinate system; (b) The measurement results of position when cutting-head move around the axis (Z_1) in rotary joints coordinate system.

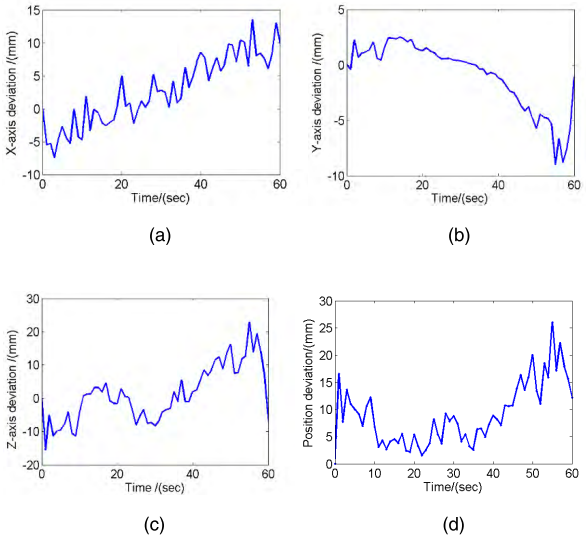

FIGURE 20. The position measurement error when cutting-head move around the axis (Z_2) in lift joints coordinate system. (a) Position measurement deviation in the X-axis direction. (b) Position measurement deviation in the Y-axis direction. (c) Position measurement deviation in the Z-axis direction. (d) Position measurement deviation where Position is $\sqrt{X^2 + Y^2 + Z^2}$.

Fig. 20 and Fig.21 show the position measurement errors, and it can be deduced that the maximum position error value is 26.01 mm. The error value is reasonable for the position measurement of the cutting-head for Boom-type roadheader. Control the cutting-head to move in diagonal lines motion path and S-shaped motion path, respectively. The proposed method and the Vicon tracker were used to measure the trajectory of cutting-head at the same time, Fig. 22 and Fig. 23 shows the trajectory of the cutting-head and its projection in the plane. It can be observed from the figure that the proposed method exhibits good performance, as the trajectory measured by the proposed method was close to that measured by the Vicon tracker.

It can be seen from Fig. 19, 22 and 23, the trajectory measured by the proposed method is close to that measured by the Vicon tracker. It can be observed also from the Fig. 20 and Fig. 21 that the maximum position measurement error of cutting-head was 26.01 mm. According to the rule that the allowed position measurement error of cutting-head in underground coal mine roadway construction is within 50mm, therefore the proposed visual measurement method can meet

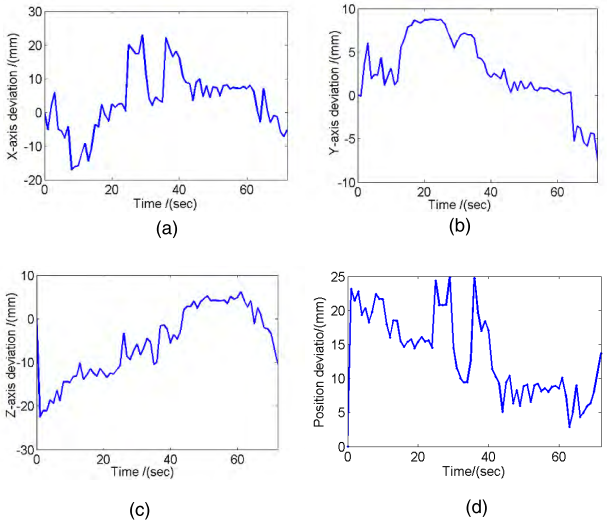

FIGURE 21. The position measurement error when cutting-head move around the axis (Z_1) in rotary joints coordinate system. (a) Position measurement deviation in the X-axis direction. (b) Position measurement deviation in the Y-axis direction. (c) Position measurement deviation in the Z-axis direction. (d) Position measurement deviation where Position is $\sqrt{X^2 + Y^2 + Z^2}$.

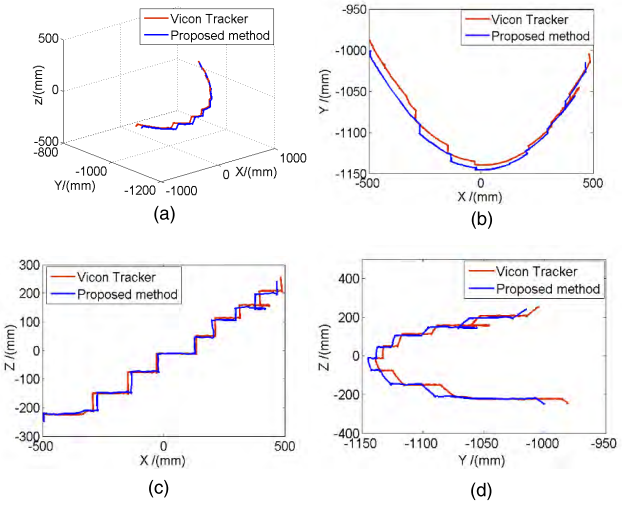

FIGURE 22. The trajectory of the cutting-head and its projection in the plane when cutting-head move in the diagonal lines motion path. (a) The trajectory of the cutting-head when its move in the diagonal lines motion path. (b) The trajectory of the cutting-head projected in the XY plane. (c) The trajectory of the cutting-head projected in the XZ plane. (d) The trajectory of the cutting-head projected in the YZ plane.

the requirement for position measurement of the cutting-head for Boom-type roadheader.

In addition, according to the cutting-head pose estimation error model proposed in Section V and the simulation evaluation results in section VI, the vision measurement system error mainly caused by the spot center location error of feature points, the non-coplanar error of the infrared LEDs and the external parameters calibration error, the position measurement errors under the influence of the three factors is within 20.72 mm. The pose measurement error is nearly identical to the theoretical analysis result, which verify the

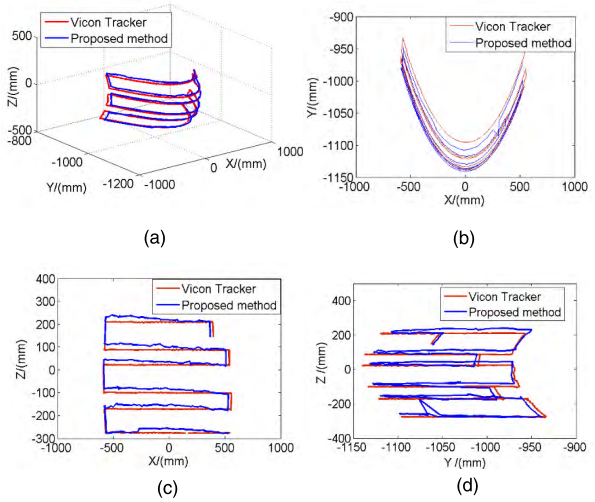

FIGURE 23. The trajectory of the cutting-head projected in the plane when cutting-head move in the S-shaped motion path. (a) The trajectory of the cutting-head when its move in the S-shaped motion path. (b) The trajectory of the cutting-head projected in the XY plane. (c) The trajectory of the cutting-head projected in the XZ plane. (d) The trajectory of the cutting-head and its projection in the YZ plane.

effectiveness of the pose measurement method for cutting-head and the error transfer model proposed in this paper.

VIII. CONCLUSION

This paper proposed a monocular vision-based cutting head pose estimation method. The infrared LEDs-based pose estimation system design and associated critical issues including underground camera model theory, pose optimal estimation algorithms and cutting-head pose estimation error modeling were studied. The above three main precision safeguard technologies were focused and the simulation and experiments were carried out to evaluate and validate the theoretical findings.

The specially designed 16-point infrared LED target has been demonstrated to be in the ability to be recognized and distinguish under extremely low illuminance and dense-dust coal mine environment. Moreover, a narrow-band filter-added camera enables the interference elimination of stray lights in tunneling faces such as visible light, laser alignment instrument, etc.

The cylinder-shaped protecting apparatus with two layer explosion-proof glasses is specially designed to prevent the dust and mist from the outer-layer glass in underground environment. Taking the angular mounting offset between the camera and the double layer glasses into the consideration, an equivalent focal length based underground camera model is established to compensate imaging error. Theoretical modeling and simulation results show that the double layer glass have a great influence on the image deviation. The farther the cutting-head is from the center of the cutting surface, the greater the error. The maximum image residuals of infrared LED are −0.47 pixel in X-axis and 0.48 pixel in Y-axis, respectively.

The improved P4P algorithm is established. Considering some of the feature points might be occluded by water mists, dense-dust, etc, the linear equations of each side of the target are firstly to be fitted by the least square fitting method, and the pixel coordinates of the four vertices of the target are calculated through the intersection of two adjacent lines. Then we transfer the P4P problem into an optimization problem and dual quaternion is introduced to establish the error objective function to obtain the optimal solution. The simulation evaluation demonstrated that the improved P4P method is with better pose estimation accuracy in comparison with the leading algorithm such as HOMO, LHM, EPNP and P4P.

The error transfer model for the three factors are established. Numerical research gives the three dimensional error distribution including the error value and error direction, which have demonstrated that the cutting-head position measurement error under the influence of the multiple factors is within 20.72mm.

The conducted experiment show that the measurement system accuracy of cutting-head position is within 26.01 mm, and the pose estimation error is nearly identical to the theoretical analysis result, which verify the effectiveness of the cutting-head pose estimation method and the error model proposed in this paper. The research of this paper provides a theoretical basis for cutting-head pose estimation in tunneling face.

The future work will be to optimize the real-time performance of the system. In addition, the error compensation method and underground camera model will be further studied and applied to improve the system measurement accuracy and reliability.

ACKNOWLEDGMENTS

Authors acknowledge the support from the students Yongwei Liu, Chao Zhang, Jianxiong Zhao, Dongman Wang and Tianlong Wang for their assistance in the experiments.

REFERENCES

[1] P. Cheng and B. Oelmann, "Joint-angle measurement using accelerometers and gyroscopes—A survey," *IEEE Trans. Instrum. Meas.*, vol. 59, no. 2, pp. 404–414, Feb. 2010. doi: 10.1109/TIM.2009.2024367.

[2] F. Ghassemi, S. Tafazoli, P. D. Lawrence, and K. Hashtrudi-Zaad, "An accelerometer-based joint angle sensor for heavy-duty manipulators," in *Proc. IEEE Int. Conf. Robot. Automat.*, May 2002, pp. 1771–1776. doi: 10.1109/ROBOT.2002.1014798.

[3] J. Tian, G. Chen, Y. Yang, H. Wang, J. Liu, and M. Wu, "Application and testing of a vertical angle control for a Boom-type road header," (in Chinese), *Mining Sci. Technol.*, vol. 20, no. 1, pp. 152–158, 2010.

[4] X. Yang, F. Zhao, and T. Chen, "NLOS identification for UWB localization based on import vector machine," *AEU-Int. J. Electron. Commun.*, vol. 87, pp. 128–133, Apr. 2018.

[5] V. R. Nuthakki and S. Dhamodharan, "UWB Metamaterial-based miniaturized planar monopole antennas," *AEU-Int. J. Electron. Commun.*, vol. 82, pp. 93–103, Dec. 2017.

[6] H. Yang, W. Li, C. Luo, J. Zhang, and Z. Si, "Research on error compensation property of strapdown inertial navigation system using dynamic model of shearer," *IEEE Access*, vol. 4, pp. 2045–2055, 2016. doi: 10.1109/ACCESS.2016.2565638.

[7] H.-C. Chang, Y.-L. Hsu, S.-C. Yang, J.-C. Lin, and Z.-H. Wu, "A wearable inertial measurement system with complementary filter for gait analysis of patients with stroke or Parkinson's disease," *IEEE Access*, vol. 4, pp. 8442–8453, 2017. doi: 10.1109/ACCESS.2016.2633304.

[8] D. Caruso, A. Eudes, M. Sanfourche, D. Vissière, and G. L. Besnerais, "A Robust indoor/outdoor navigation filter fusing data from vision and magneto-inertial measurement unit," *Sensors*, vol. 17, no. 12, p. E2795, 2017.
[9] E. Duff, "Tracking a vehicle from a rotating platform with a scanning range laser," in *Proc. Austral. Conf. Robot. Automat.*, Melbourne, VIC, Australia, 2006, p. 12.
[10] A. Kashani, W. Owen, N. Himmelman, P. Lawrence, and R. Hall, "Laser scanner-based end-effector tracking and joint variable extraction for heavy machinery," *Int. J. Robot. Res.*, vol. 29, no. 10, pp. 1338–1352, 2010. doi: 10.1177/0278364909359316.
[11] M. Wu *et al.*, "Autonomous measurement of position and attitude of Boom-type roadheader based on space intersection measurement," (in Chinese), *J. China Coal Soc.*, vol. 40, pp. 2596–2602, Nov. 2015. doi: 10.13225/j.cnki.jccs.2015.7065.
[12] M. Fiala, "ARTag, a fiducial marker system using digital techniques," in *Proc. IEEE Comput. Soc. Conf. Comput. Vis. Pattern Recognit. (CVPR)*, Washington, DC, USA, vol. 2, Jun. 2005, pp. 590–596.
[13] C. Fenga, V. R. Kamat, and H. Cai, "Camera marker networks for articulated machine pose estimation," *Automat. Construction*, vol. 96, pp. 148–160, Dec. 2018.
[14] C.-P. Lu, G. D. Hager, and E. Mjolsness, "Fast and globally convergent pose estimation from video images," *IEEE Trans. Pattern Anal. Mach. Intell.*, vol. 22, no. 6, pp. 610–622, Jun. 2000.
[15] Y. Abdel-Aziz, H. Karara, and M. Hauck, "Direct linear transformation from comparator coordinates into object space coordinates in close-range photogrammetry," *Photogram. Eng. Remote Sens.*, vol. 81, no. 2, pp. 103–107, 2015.
[16] S. Malik and G. Roth, "Robust 2D tracking for real-time augmented realit," in *Proc. Vis. Interface Conf.*, 2002, pp. 399–406.
[17] V. Lepetit, F. Moreno-Noguer, and P. Fua, "EP*n*P: An accurate O(*n*) solution to the P*n*P problem," *Int. J. Comput. Vis.*, vol. 81, no. 2, pp. 155–166, 2009.
[18] S. Li, C. Xu, and M. Xie, "A robust O(*n*) solution to the perspective-*n*-point problem," *IEEE Trans. Pattern Anal. Mach. Intell.*, vol. 34, no. 7, pp. 1444–1450, Jul. 2012.
[19] G. Telem and S. Filin, "Photogrammetric modeling of underwater environments," *ISPRS J. Photogram. Remote Sens.*, vol. 65, no. 5, pp. 433–444, Sep. 2010.
[20] G. Telem and S. Filin, "Photogrammetric modeling of the relative orientation in underwater environments," *ISPRS J. Photogramm. Remote Sens.*, vol. 86, pp. 150–156, Dec. 2013.
[21] J. C. Trinder, J. Jansa, and Y. Huang, "An assessment of the precision and accuracy of methods of digital target location," *ISPRS J. Photogramm. Remote Sens.*, vol. 50, no. 2, pp. 12–20, Apr. 1995.
[22] H. Zhang *et al.*, "Accurate star centroid detection for the advanced geosynchronous radiation imager of fengyun-4A," *IEEE Access*, vol. 6, pp. 7987–7999, 2018.
[23] F. Xinxing, Z. Liyan, and Y. Nan, "Fast algorithms on center location of two dimensional Gaussian distribution spot. Acta optica sinica," (in Chinese), *Acta Optica Sinica*, vol. 32, no. 5, 2012, Art. no. 0512002. doi: 10.3788/AOS201232.0512002.
[24] H. Dong and L. Wang, "Non-iterative spot center location algorithm based on Gaussian for fish-eye imaging laser warning system," *Optik*, vol. 123, no. 23, pp. 2148–2153, Dec. 2012.
[25] M. A. Abidi and T. Chandra, "A new efficient and direct solution for pose estimation using quadrangular targets: Algorithm and evaluation," *IEEE Trans. Pattern Anal. Mach. Intell.*, vol. 17, no. 5, pp. 534–538, May 1995.
[26] M. W. Walker, L. Shao, and R. A. Volz, "Estimating 3-D location parameters using dual number quaternions," *CVGIP, Image Understand.*, vol. 54, no. 3, pp. 358–367, Nov. 1991.
[27] B. Qiao, S. Tang, K. Ma, and Z. Liu, "Relative position and attitude estimation of spacecrafts based on dual quaternion for rendezvous and docking," *Acta Astronautica*, vol. 91, pp. 237–244, Oct./Nov. 2013.
[28] K. Fathian, J. Jin, S.-G. Wee, D.-H. Lee, Y.-G. Kim, and N. R. Gans, "Camera relative pose estimation for visual servoing using quaternions," *Robot. Auton. Syst.*, vol. 107, pp. 45–62, Sep. 2018.
[29] P. Wang, G. Xu, Y. Cheng, and Q. Yu, "A simple, robust and fast method for the perspective-*n*-point problem," *Pattern Recognit. Lett.*, vol. 108, pp. 31–37, Jun. 2018.

WENJUAN YANG received the B.S. and M.S. degrees in mechatronic engineering from the Xi'an University of Science and Technology, Xi'an, China, in 2012 and 2015, respectively, where she is currently pursuing the Ph.D. degree in mechatronic engineering. Her research interests include image processing, vision measurement, vision-based position measurement, and accurate location of mobile equipment underground coal mine.

XUHUI ZHANG received the B.S. degree from the Xi'an Mining Institute, Xi'an, China, in 1996, the M.S. degree from the Xi'an University of Science and Technology, Xi'an, in 2002, and the Ph.D. degree in instrument science and technology from Xi'an Jiaotong University, in 2009. He is currently a Professor and Ph.D. Supervisor with the Xi'an University of Science and Technology. His research interests include vision measurement, vision-based position measurement, and accurate location of mobile equipment, conditional monitoring, and fault diagnosis.

HONGWEI MA received the B.S. and M.S. degrees in mechatronic engineering from the Xi'an Mining Institute, Xi'an, China, in 1984 and 1993, respectively, and the Ph.D. degree in mechanical engineering from Xi'an Jiaotong University, Xi'an, in 1998. He is currently a Professor and Ph.D. Supervisor with the Xi'an University of Science and Technology. His research interests include image processing and pattern recognition, special intelligent robot, and nondestructive testing and evaluation.

GUANG-MING ZHANG received the M.Sc. and Ph.D. degrees in mechanical engineering from Xi'an Jiaotong University, Xi'an, China, in 1996 and 1999, respectively. He joined the Institute of Acoustics, Nanjing University, in 1999. From 2001 to 2003, he was with the Signals and Systems Group, Uppsala University, Sweden, as a Postdoctoral Fellow. He is currently with Liverpool John Moores University, U.K., where he is currently an Associate Professor of ultrasonic engineering. His current research interests include reliability testing and failure analysis of modern microelectronic packages, ultrasonic signal and image processing, ultrasonic non-destructive testing and evaluation, and prognostics and health management of electronics.